PAPER

Melamine-derived N-rich C-entrapped Au nanoparticles for sensitive and selective monitoring of dopamine in blood samples†

Faria Shakeel,[a] Muhammad Waseem Fazal,[b] Anam Zulfiqar,[c] Farhan Zafar,[b] Naeem Akhtar, [ID] *[b] Arsalan Ahmed,[b] Hafiz Badaruddin Ahmad,*[a] Safeer Ahmed, [ID] [d] Asad Syed,[e] Ali H. Bahkali,[e] Muhammad Abdullah [ID] [f] and Zahid Shafiq [ID] *[ag]

Several neurological disorders, including Parkinson's disease, schizophrenia, human immunodeficiency virus infection, and restless leg syndrome, majorly result from disruption in the dopamine (DA) level. Thus, useful information about the treatment and prevention of various genetic majorly mental health problems can be obtained through precise and real-time monitoring of DA. Herein, we report the fabrication of novel N-rich carbon-coated Au nanoparticles (NC@Au-NPs) by deriving from melamine-crosslinked citrate-stabilized Au NPs. NC@Au-NPs offer fast electro-oxidation efficacy towards DA, because of strong electrostatic attraction between negatively charged NC@Au-NPs and positively charged DA. The catalytic efficacy and shelf life of the designed system were further boosted by applying a mixture of polydopamine (PDA) and benzimidazolium-1-acetate ionic liquid (IL) as a sandwich between the working electrode surface (graphitic pencil electrode: GPE) and the designed nanohybrid NC@Au-NPs as a redox mediator. The results indicate that the designed novel NC@Au/PDA−IL/GPE exhibits excellent sensitivity, selectivity, and reproducibility over a wide linear range (50−1000 nm) and a low detection limit of 0.002 μM ± 0.001 as well. The developed sensor was successfully applied to monitor DA in the blood of COVID-19 quarantined patients and pharmaceutical samples with high accuracy, thus suggesting a powerful tool for the diagnosis of mental problems.

1. Introduction

The coronavirus disease-2019 (COVID-19) pandemic has seriously affected people worldwide causing severe acute respiratory syndrome.[1] Several nonpharmacological interventions have been applied by health organizations and ministries at the start of the pandemic when no definite treatment was available.[2] These interventions include physical distancing, quarantine of

[a]*Institute of Chemical Sciences, Bahauddin Zakariya University, Multan 60800, Pakistan. E-mail: zahidshafiq@bzu.edu.pk; hafizbadar@googlemail.com*

[b]*Interdisciplinary Research Centre in Biomedical Materials (IRCBM), COMSATS University Islamabad, Lahore Campus, Lahore 54000, Pakistan. E-mail: naeemkhan@cuilahore.edu.pk*

[c]*Department of Biochemistry, Bahauddin Zakariya University, 60800, Multan, Pakistan*

[d]*Department of Chemistry, Quaid-i-Azam University, 45320, Islamabad, Pakistan*

[e]*Department of Botany and Microbiology, College of Science, King Saud University, P. O. 2455, Riyadh, 11451, Saudi Arabia*

[f]*Department of Chemistry, University of Massachusetts Amherst, 710 North Pleasant Street, Amherst, Massachusetts 01003, USA*

[g]*Department of Pharmaceutical & Medicinal Chemistry, An der Immenburg 4, D-53121 Bonn, Germany*

† Electronic supplementary information (ESI) available. See https://doi.org/10.1039/d2ra02754b

exposed individuals, travel restrictions, closure of schools and workplace, cancellation of mass gatherings, and use of personal protective equipment.[3] Even though these strategies had a significant effect in controlling the COVID-19 outbreak and helped reducing its transmission, they had a very strong negative impact on people's mental health.[4] It has been reported that various neurological disorders such as delirium, agitation, confusion, depression, anxiety, and traumatic stress symptoms appeared in quarantined, isolated, and even in COVID-19 survivors.[5] The appearance of these neurological disorders could be due to alteration in neurotransmitters.[6–8] Neurotransmitters are chemical messengers that control both psychological and physiological functions of the body.[9,10] Dopamine (DA) is a common catecholamine neurotransmitter found in mammals' central peripheral neural system, body fluids, and brain tissues.[11] The normal range of DA in a healthy body is in the range of 1.3–2.6 μM.[12] However, any fluctuation from the normal range may lead to severe immunological and neurological disorders such as hypertension, heart failure, Parkinson's, schizophrenia, epilepsy, human immune deficiency syndrome, neuromuscular disorders, and even depression.[13] Recently, it has been observed that the rate of fluctuation in the concentration of DA in depressed patients has increased after the COVID-19 outbreak.[14] Thus, precise monitoring of the DA

level in blood samples of COVID-19 quarantined patients with excellent accuracy is of great concern not only for clinical diagnosis of various neurological disorders but for treatment as well.

To date, numerous analytical techniques such as chemiluminescence, capillary electrophoresis, spectroscopic methods, calorimetry, high-performance liquid chromatography, mass spectrometry, and electrochemical analysis have been successfully implemented for DA detection.[8,9] Among these, the electrochemical strategy has gained great interest because of its low cost, fast and facile nature, nippy response, simplicity, cost-efficiency, high sensitivity, selectivity, lower detection limit, and reliability.[9,15,16] Moreover, the onsite multiple analyte detection is also compelling to make the advancement in portable electrochemical sensing devices. For instance, a wide range of tailor-made single and multi-component metals such as reduced graphene oxide sheet AuNP complexes have been successfully designed to determine DA.[17] Similarly, AuNP-anchored nitrogen-doped graphene has been synthesized by a seed-assisted growth methodology and shows sensitive and selective efficacy towards DA and glucose.[18] Recently, Mahalakshmi *et al.* used an electrodeposition strategy to design a AuNP-coated polyaniline-modified glassy carbon electrode for the selective monitoring of DA.[19] Furthermore, a three-layer composite of AuNPs, choline, and graphene quantum dot-based carbon fiber microelectrodes has been developed for the highly sensitive monitoring of DA without interference from AA.[20]

Even though most of these exhibit excellent selective features, fabrication of low-cost and easy-to-handle sensing probes with exceptional sensitivity, selectivity, and reproducibility remains a big challenge for developing a portable electrochemical sensor for real-time applicability. Moreover, electrochemical sensing performance is mainly associated with the composition and morphology of the electrode material. However, constructing nanohybrid electrode materials with controllable shape, size and composition is quite complicated.[21] To overcome these bottlenecks, various strategies such as development of binder-free *in situ* fabrication of nanohybrids not only to enhance reproducibility but also to increase the electrode–electrolyte interaction[22] and coating the electrode material with an electron transport or redox mediator to boost the shuttling of electrons at the interface have been adopted. Recently, we have successfully minimized this issue by wrapping the designed material with highly efficient electron transport mediators such as C-dot/N-rich graphitic C, even without perturbing its shape and size.[21,23] Despite these, it is still necessary to improve the intrinsic features such as charge carrier densities, thermal and electrochemical stability, and surface interaction to facilitate the smooth transportation of molecules at their specific oxidation potential to achieve not only high sensitivity but selectivity and reproducibility as well.

In this work, we synthesized novel nitrogen (N)-rich graphitic carbon (C)-coated Au-NPs (NC@Au) by deriving from melamine-crosslinked citrate-stabilized Au-NPs. The melamine-derived N-rich C improves the electrocatalytic efficacy of Au-NPs by exposing more fraction of catalytic active sites. Moreover, to

boost the intrinsic features, a mixture of polydopamine (PDA) and benzimidazolium-1-acetate ionic liquid (IL) has been sandwiched between the working electrode surface (graphitic pencil electrode: GPE) and the designed nanohybrid (NC@Au) as a redox mediator. The provided redox mixture (rich in electron density) offers not only efficient adsorption capability to NC@Au at the GPE to improve the electrochemical stability and reproducibility but also smooth and fast shuttling of ions/molecules at their specific oxidation potential to achieve excellent selectivity. Interestingly, the designed novel NC@Au/PDA–IL/GPE sensor shows excellent sensitivity and selectivity with a reliable shelf life for DA screening. The designed sensor shows a wide linear range (50–1000 nm) with a detection limit of 0.002 μM ± 0.001. Because of high selectivity and sensitivity, the developed sensor was further successfully applied to monitor DA in the blood of COVID-19 quarantined patients and pharmaceutical samples. According to our knowledge, this is the first report to use a novel design based on NC@Au/PDA–IL/GPE sensors to monitor DA in COVID-19 quarantined patients and pharmaceutical samples with reliable reproducibility, excellent sensitivity, and selectivity.

2. Experimental

2.1 Chemicals and reagents

Phosphate buffer saline (PBS), sodium chloride (NaCl), melamine, potassium ferricyanide, DA, uric acid (UA), ascorbic acid (AA), lactose, KCl, NaCl, Na_2SO_4 and K_2SO_4 were purchased from Sigma-Aldrich. Sodium sulfate and benzimidazole were purchased from Aladdin. Gold(III) chloride trihydrate, silver nitrate, sodium borohydride, cetyltrimethylammonium bromide, and all other chemical reagents were used directly without further purification and purchased from Sigma-Aldrich. A pH meter was used to prepare buffer solutions of different pH values with 0.1 M NaH_2PO_4.

Human blood sample was obtained from a 30 year-old COVID-19 quarantined volunteer. Dopamine hydrochloride injection (10 mg mL^{-1}, 2 mL per injection) was purchased from a local medical store. Deionized water from a Millipore Q water purification system was used in all experiments.

2.2 Synthesis of citrate-stabilized Au-NPs

AuNPs were synthesized by using the already reported strategy.[24] Briefly, in the first step, a Au seed solution was prepared by mixing 5 mL of 0.2 M cetyltrimethylammonium bromide (CTAB) with 5 mL of 0.5 mM $HAuCl_4 \cdot 3H_2O$. After that, 0.6 mL of 0.01 mM $NaBH_4$ was added dropwise, and the solution was kept under stirring for two minutes, which resulted in the formation of a Au seed solution. In the second step, the as-prepared Au seed solution was poured into a solution prepared by mixing CTAB (30 mL, 0.2 M), $HAuCl_4 \cdot 3H_2O$ (30 mL, 1 mM), $AgNO_3$ (1.5 mL, 4 mM) and AA (0.5 mL of 0.2 M). AA acts as a reducing agent, thus turning growth solution from dark yellow to colorless. Finally, the solution was incubated at 30 °C overnight, which results in the formation of Au-NPs. Au-NPs were further centrifuged and washed with deionized water at

10 000 rpm for 30 minutes to remove impurities and by-products.

2.3 Synthesis of NC@Au-NPs and IL

To wrap the surface of Au-NPs with NC, we used the already reported strategy. Briefly, melamine was chosen as a source because of its high N content and easy binding at the surface *via* coordinate interaction.[25] Typically, 100 mg of as-synthesized Au-NPs were homogeneously dispersed under ultrasonication for 6 h in 100 mL of Tris buffer solution and then loaded into a 250 mL volumetric flask and kept under stirring at room temperature. After that, melamine was added, and the solution was kept under stirring at room temperature for 12 h for proper adsorption. After the given time, melamine-wrapped Au-NPs were subjected to washing with deionized water and ethanol. Finally, to get desired NC-wrapped Au-NPs, the already dried powder of melamine-wrapped Au-NPs was calcined at 450 °C for 5 h. Similarly, a benzimidazolium-1-acetate ionic liquid (IL) was prepared (Fig. S2†) by following the procedure already reported in the literature[21] and characterized by NMR (Fig. S1 and S2†) and FTIR (Fig. S3†).

2.4 Fabrication of PDA–IL-wrapped GPE

For the fabrication of a PDA–IL-wrapped graphitic pencil electrode (GPE), the first solution of DA was prepared by mixing DA (4 mg) in phosphate buffer (100 mL) in a 250 mL flask and kept under stirring for 2 min at room temperature. GPE was dipped into a stirring solution and kept for 4 h. DA-polymerized GPE was washed several times with DI (deionized) water. After this, polymerized GPE was dipped for 1 h into another solution of IL. Finally, the PDA–IL-wrapped GPE was washed with DI water and dried at room temperature for 2 h.

2.5 Fabrication of sensing probes

A conventional three-electrode system was used, which consists of a GPE of 40 mm length and 0.5 mm diameter as the working electrode, Ag/AgCl as the reference electrode, and a Pt wire as the counter electrode. For an electrical contact, one end of the lead pencil was attached to a copper wire and put into a tube carrying araldite (epoxy resin, 1 : 1). The PDA–IL-wrapped GPE was coated with the synthesized material by a simple dip-coating method. First, the solution was prepared by adding 2 mg of synthesized material to 1 mL L^{-1} DI water separately and then subjecting to ultrasonication for 2 h to obtain a uniform solution for the fabrication of the desired working electrode. Then, the PDA–IL-wrapped GPE was immersed in this solution for 24 h at room temperature. The modified electrode was then allowed to dry for 24 h and to get a smooth and clean surface, the prepared electrode was gently washed with DI water to remove the loosely bound material. The as-prepared electrode was next used for electrochemical analysis. All the electrodes were prepared in the same manner by using equal concentrations under the same environmental condition to get reliable comparative results.

3. Results and discussion

3.1 Morphological and compositional analysis of NC-wrapped Au-NPs

Electrocatalytic activity and properties of NPs are highly dependent upon their shape, size, and composition offering highly sensitive and selective monitoring towards the analyte. Transmission electron microscopy (TEM) analysis was employed to explore the surface morphology of Au and NC@Au-NPs. TEM images with low and high magnifications are shown in Fig. 1, which reveal the uniform formation of spherical shaped NPs over a wide range for both Au (A and B) and NC@Au-NPs (C and D). The size of NPs was confirmed using automatic software (*e.g.*, ImageJ) and observed to be in the range of 20–25 and 20–30 nm for Au and NC@Au-NPs, respectively. The inset of Fig. 1D clearly shows the formation of NC coating at the surface of Au-NPs, with thickness in the range of 3–5 nm.

The composition of the synthesized Au and NC@Au-NPs was observed by X-ray diffraction (XRD) analysis. The XRD analysis of the as-synthesized Au and NC@Au-NPs shows well-resolved and clear diffraction peaks (Fig. 2A). The diffraction bands at 2θ values of 38°, 44°, 64°, and 77° could be attributed to (1 1 1), (2 0 0), (2 2 0), and (3 1 1) Bragg's reflection planes of metallic Au cubic structures, which matches well with JCPDS no. 04-0784. The additional peak in the case of NC@Au-NPs at around 22.84° (002) could be attributed to graphitic C. Based on the XRD results, the average crystallite size and strain of Au and NC@Au-NPs were also calculated using Scherrer and Williamson–Hall equations,[26] respectively (Section S5 and Table S1†). The results indicate that NC@Au-NPs (3.20 nm) have a lower crystallite size
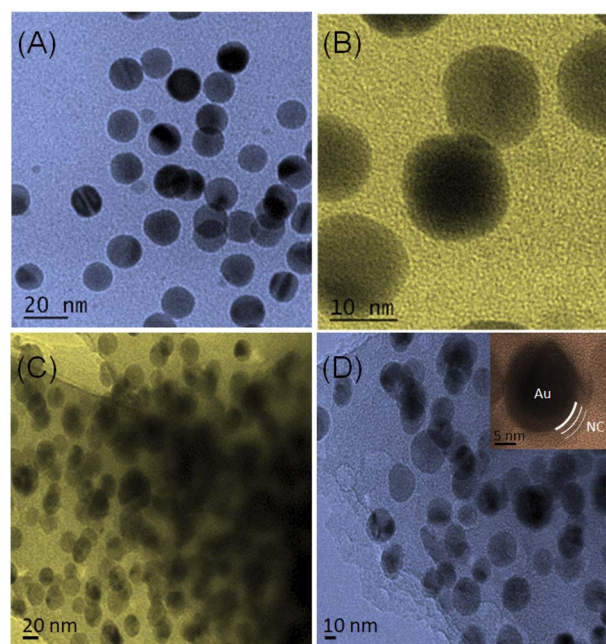

Fig. 1 (A and C) Low- and (B and D) high-magnification TEM images of AuNPs and NC@AuNPs, respectively, illustrating the surface morphology and symmetric distribution with a spherical shape. The inset in (D) shows the clear formation of the NC layer on AuNPs.
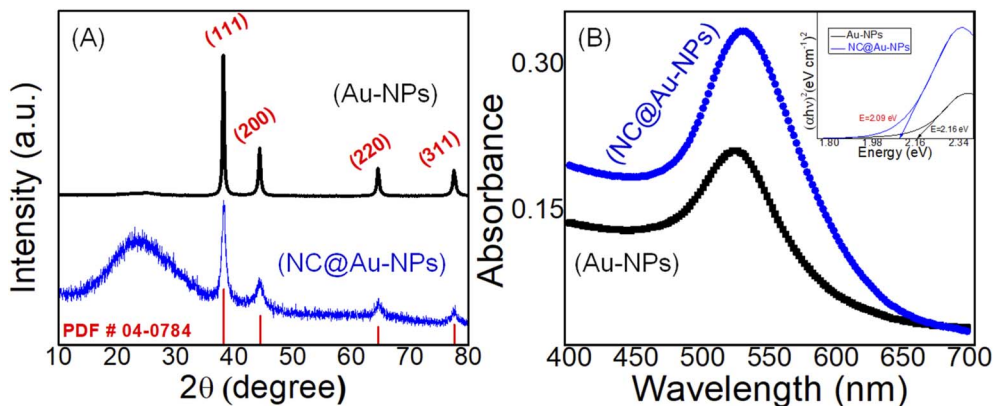
Fig. 2 (A) XRD and (B) UV–Vis spectrum of Au–NPs (black line) and NC@Au–NPs (blue line), respectively. The inset in (B) shows the Tauc plot derived from UV spectra.

than that of the Au-NPs (17.20 nm). Furthermore, Raman analysis of NC@Au-NPs (Fig. S4A†) shows a prominent band at 495 cm^{-1}, indicating the existence of the ν (metal-O) band, thus confirming the presence of the Au metal.[27] The presence of Raman bands at around 712 cm^{-1} reveals the C–C skeletal vibration, thus confirming the presence of melamine. Additionally, the existence of 2 extra peaks at ~1334 and 1630 cm^{-1} confirms the presence of the D and G bands respectively. The D band represents the defect-rich disordered carbon, whereas the G band shows the existence of sp^2 clusters at the surface of Au-NPs.[28]

The impact of NC wrapping on the stability and size of Au-NPs was further confirmed by ultraviolet-visible spectroscopy. The UV spectra of both Au and NC@Au-NPs show an absorption band in the visible array of 524 and 529 nm, respectively (Fig. 2B). The small difference in peak position could be attributed to the difference in the size of NPs. The sharpness of NC@Au-NPs and Au-NPs was calculated *via* full width at half maximum (FWHM). The results (Table S3†) indicate that no significant difference in the sharpness of both NC@Au-NPs and Au-NPs was observed.

The band gap of the Au and NC@Au-NPs was next calculated by the Tauc and Davis–Mott relationship[29] using UV data (inset Fig. 2B and Section S6†). The results indicated that a band gap of Au-NPs (2.16 eV) decreases after coating or wrapping with the NC (2.09 eV), thus suggesting strong interaction between Au and NC. Additionally, the overall charge at the surface of Au-NPs and NC@Au-NPs was further investigated by zeta potential (Fig. S4B†). The zeta potential of Au-NPs and NC@Au-NPs was observed to be −38.2 and −27.4 mV, respectively.

The binding interaction of the electrode material at the surface of the electrode was thoroughly investigated. Briefly, the oxidation of DA in the buffer electrolyte leads to its self-polymerization and formation of PDA at the surface of GPE. The amino groups at the surface of PDA further bind with the acetate of the IL *via* ionic linkage. Melamine has different binding sites including exocyclic amino groups and nitrogen-containing rings, which binds with AuNPs. Dip coating of NC@Au-NPs results in H-bonding between IL and NC-based Au-

NPs. The IL interaction with NC@Au-NPs is also evident from the FTIR spectra (Fig. S5†) clearly showing the in-plane vibration of C–C (1592 cm^{-1}), thus indicating the clear existence of benzimidazolium along with the characteristic absorption band of Au (653.28 cm^{-1}). Additionally, the peak at 1409 cm^{-1} is assigned to the asymmetric and symmetric C–H scissoring vibrations of the CH$_3$–N$^+$ moiety and clearly shows the presence of H-bonding between AuNPs and IL, which is in accordance with the reported literature.[30] The IL contributes to the π-electron density of the system enhancing the speed of electron transfer due to a smooth conductive pathway. The results of UV and Raman spectra confirm these interactions within the system. The interactions of the IL with PDA and NC@Au-NP are shown in Scheme 1.

3.2 Impact of redox mediator (PDA and PDA–IL) on the electrochemical behaviour of Au and NC@Au-NP-based electrodes

The impact of electron transport mediators or redox mediators such as PDA and IL on the electrocatalytic and charge transfers kinetics of Au (Fig. 3A) and NC@Au-NPs (Fig. 3B) was evaluated
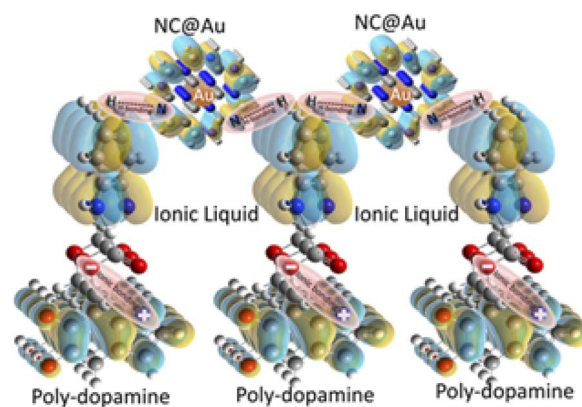
Scheme 1 Schematic illustration showing the interaction between the species such as poly-dopamine, ionic liquid, and NC@Au-NPs, coated at the surface of GPE.

by cyclic voltammetry (CV) measurements in phosphate buffer (pH 7.0) against 2 mM of $[Fe_6]^{3-/4-}$ (ref. 31) at an applied potential range of −0.6 to 0.6 V (vs. Ag/AgCl) under 100 mV s^{-1} scan rate. We used a redox probe $[Fe_6]^{3-/4-}$ (ref. 31) to have a careful look at various factors including kinetic, electronic, and surface properties of designed electrodes. The CV plots of all electrodes including Au, Au/PDA, Au/PDA–IL, NC@Au, NC@Au/PDA, and NC@Au/PDA–IL show redox peaks, thus suggesting their electrocatalytic capability. However, the NC@Au-NP-based GPE exhibits enhanced electrocatalytic efficacy by showing low peak-to-peak potential value and high peak current compared to Au-NPs-based GPE (Table S4†). The electrocatalytic efficacy of both electrodes increased further when the PDA-coated GPE was applied and surprisingly became double when a mixture of PDA/IL was applied as an electron transport or redox mediator.

Similarly, electrochemical impedance spectroscopy (EIS) was also employed to investigate the interfacial electron transfer capability of Au (Fig. 3C) and NC@Au-NP (Fig. 3D)-based electrodes using 2 mM of $[Fe_6]^{3-/4-}$ (ref. 31) as a redox probe. The EIS curve displayed two useful properties: (i) semicircle diameter which represented the electrode's electron resistance at high frequencies, and[22] a line which represented electron diffusion at low frequencies. The Nyquist plot revealed that the NC@Au-NP-based electrode has low semicircle and low charge transfer resistance with high electrical conductivity compared to its counterpart (Au-NPs-based electrode). The charge transfer resistance decreased proportionally upon applying electron transport mediator PDA and PDA/IL, respectively. These results suggest enhanced ion shuttling capability of the NC@Au-NP-based electrode compared to Au-NPs at the electrode–electrolyte interface by exposing a greater fraction of catalytic active sites more smoothly, and[22] the strong binding interaction (H-bonding) of the redox mediator (PDA/IL) with the coated material (Au or NC@Au), which not only acted as a binding support but also offered fast and smooth pathways for fast transportation of ions.

The impact of the redox mediator on the ion transportation rate was further confirmed by calculating the diffusion coefficient (D) through the Cottrell equation (eqn (1)). The chronoamperometric measurements (Fig. S6†) were used to calculate the D.

$$I_t = nFAD^{1/2}C\pi^{-1/2}t^{-1/2} \tag{1}$$

where F is the Faraday constant (96 485 C mol^{-1}), A is the geometric surface area of the electrode (0.03 cm^2), I_t (56.5 μA) is the current in the presence of 1 mM $[Fe_6]^{3-/4-}$ (ref. 31), D is the diffusion coefficient (cm^2 s^{-1}), C is the analyte concentration (0.001 mol cm^{-3}), and t is the elapsed time (311 s). The value of D was observed to be 3.4×10^{-3}, 1.58×10^{-3}, and $1.004 10^{-3}$ cm^2 s^{-1} for NC@Au-NPs/PDA–IL, NC@Au-NPs/PDA, and NC@Au-NPs electrodes, respectively. In the same manner, the value of D was also observed to be 8.5×10^{-4}, 3.6×10^{-4}, and 2.75×10^{-3} cm^2 s^{-1} for Au-NPs/PDA–IL, Au-NPs/PDA, and Au-NPs, respectively.

Moreover, to validate the enhanced ion shuttling capability of NC@Au-NPs compared to Au-NPs, we next applied the Randles–Sevcik method (eqn (2)) to calculate the interfacial active surface area of the electrode.[32]
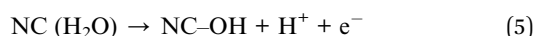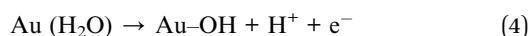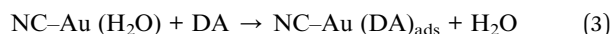
$$I_p = 2.69 \times 10^5 An^{3/2}D^{1/2}C \times v^{1/2} \tag{2}$$

where A is the interfacial active surface area of the electrode, I_p represents the anodic peak current, n indicates the number of electrons involved which is equal to 1 for $[Fe_6]^{3-/4-}$ (ref. 31), C indicates the concentration while v represents the scan rate. D is the diffusion coefficient and its value is 3.4×10^{-3} cm^2 s^{-1}, as we calculated by applying the Cottrell equation (eqn (1)). Upon substitution of these values, the calculated interfacial active surface area of Au-NPs (0.14 cm^2) was observed to be much lower than the NC@Au-NPs (0.26 cm^2). These results indicate the existence of a greater fraction of catalytic active sites at the surface of NC@Au-NPs.

### 3.3 Electrocatalytic efficacy of NC@Au-NPs/PDA/IL-based electrodes toward DA monitoring

CV measurements were carried out to examine the electrocatalytic efficacy of the fabricated NC@Au-NPs/PDA/IL-based electrode towards DA in 0.1 M PBS (pH: 7.0) at 100 mV s^{-1}. It is obvious from Fig. 3E that a redox peak appears at the surface of the designed electrode upon the addition of 5 μM of DA, and the peak current increases further towards increasing doses of DA (10, 20 μM). The results further indicated that the developed electrode has a high peak current (6.30 μA) and a low peak potential difference (ΔE = 0.12 V), suggesting enhanced electrocatalytic oxidation activity efficacy towards DA in terms of reversible redox reaction and fast electron transfer capability through the increased fraction of catalytic active sites at the electrode–electrolyte interfaces. Additionally, the negatively charged NC surface further supports the adsorption of positively charged DA via strong electrostatic interaction.

Briefly, the electro-oxidation of DA is mainly dependent upon the formation of DA-quinone (DAQ) species at the surface of NC@Au-NPs/PDA/IL (Scheme 2). As the NC@Au-NPs/PDA/IL electrode is dipped into the electrolyte, different oxygenated species will appear on the surface of AuNPs and NC.[33] These oxygenated species will result in the oxidation of DA to DAQ. The proposed mechanism is as follows.

$$\text{NC–Au (H}_2\text{O)} + \text{DA} \rightarrow \text{NC–Au (DA)}_{ads} + \text{H}_2\text{O} \tag{3}$$

$$\text{Au (H}_2\text{O)} \rightarrow \text{Au–OH} + \text{H}^+ + \text{e}^- \tag{4}$$

$$\text{NC (H}_2\text{O)} \rightarrow \text{NC–OH} + \text{H}^+ + \text{e}^- \tag{5}$$

$$\text{Au (DA)}_{ads} + \text{Au–OH} + \text{NC–OH} \rightarrow \text{DAQ} + \text{Au} + \text{NC} + n\text{e}^- \tag{6}$$

The experimental conditions including pH and applied potential have a strong impact on the sensing and selective performance of the designed electrode, thus these parameters
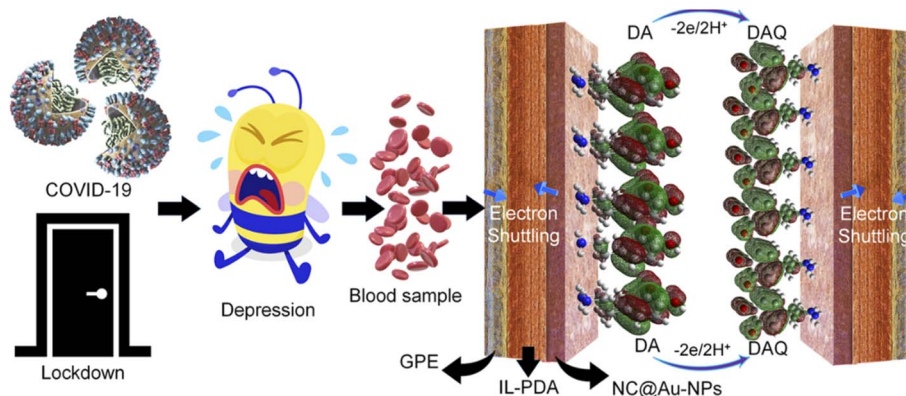
Scheme 2 Schematic illustration showing the adsorption and oxidation of DA derived from the blood of COVID-19 quarantined depressed patients, at the surface of the designed NC@Au-NPs/PDA/IL electrode.

were optimized. The response current gradually increased from pH 3.0 to 7.0 and then decreased over 7.0, as shown in (Fig. S7†). These results indicated that the number of electrons that evolved in the redox process was equal to the number of protons. Thus, pH 7.0 was selected as the optimal pH, which is also useful for monitoring human body physiological fluids, thus the subsequent experiments were performed at this pH. Similarly, the applied peak potential was also optimized to be applied for amperometry measurements. The results (Fig. 3F) indicate that the peak current increased rapidly upon increasing the applied potential from 0.25 to 0.32 V; however, we applied 0.26 V as the applied potential for amperometry measurements to maintain the selectivity.

3.4 Reaction kinetics and mechanistic investigations

The mechanism of interaction at the surface of the NC@Au-NPs/PDA/IL electrode was further investigated by executing CV at different scan rates (20–200 mV s^{-1}) towards 5 µM of DA in 0.1 M PBS (pH: 7), as shown in Fig. S8A.† The results indicated that redox peaks increased with an increase in scan rate value and suggested that the electro-oxidation of DA at the NC@Au-NPs/PDA/IL electrode surface is an adsorption-controlled process. The relationship between the scan rate on the x-axis and anodic and cathodic peak current on the y-axis showed a linear and positive shift, as shown in Fig. S8B.†

$$I_p = 0.0822x - 1.636, R^2 = 0.9908 \text{ (for anodic current)}$$

$$I_p = -0.0324x + 0.0273, R^2 = 0.9991 \text{ (for cathodic current)}$$

A relationship was obtained for both anodic and cathodic by plotting a graph between the anodic peak current (I_p) and the square root of the scan rate (Fig. S8C†).

$$I_p = 1.5312x - 7.985, R^2 = 0.9424 \text{ (anodic current)}$$

$$I_p = -0.6101x + 2.5922, R^2 = 0.9692 \text{ (cathodic current)}$$

Similarly, a linear relation was obtained by plotting a graph between the natural logarithm of scan rate and peak current (Fig. S8D†).

$$\ln I_p = 1.266x - 4.0064, R^2 = 0.9968 \text{ (for anodic)}$$

$$\ln I_p = -0.9675x + 3.2842, R^2 = 0.9979 \text{ (for cathodic)}$$

Moreover, the relationship between the natural logarithm of scan rate and the potential also shows a linear behavior (Fig. S8E†).

$$E_p = -0.0005x + 0.2692, R^2 = 0.2612 \text{ (for anodic)}$$

$$E_p = -0.0126x + 0.2011, R^2 = 0.9164 \text{ (for cathodic)}$$

Next, we applied the Laviron equation (eqn (7)) to determine the number of electrons involved in the reaction mechanism.

$$\text{Slope} = 2.303 \frac{RT}{\alpha n F} \quad (7)$$

Here T represents the temperature in kelvin, R shows the gas constant, α shows the electron transfer coefficient, F shows the Faraday constant whose value is 96 485 C mol^{-1}, and n represents the electron transfer number. The value of 'αn' was determined from the slope of the E_p vs. ln ν graph, as shown in Fig. S8E.† By substituting all these values, the calculated number of electrons involved in the oxidation of DA is 2.00, while the value of the electron transfer coefficient (α) is 59.13, thus suggesting a two-electron two-proton-coupled mechanism.

3.5 Sensing and selective efficacy of NC@Au-NPs/PDA/IL-based electrodes

To develop a reliable DA sensor, factors including sensitivity, stability, and selectivity are of major concern. Thus, evaluating these factors is highly recommended for constructing an electrochemical sensor. To ascertain the sensing efficacy, amperometric measurements were employed towards increasing doses (50–1000 nM) of DA at an applied potential of 0.26 V in 0.1 M

PBS (Fig. 4A). The designed electrode displayed a rapid increase in amperometric current towards increasing doses of the analyte with a fast response time (~3 s), thus suggesting high sensing efficacy of the developed electrode. Additionally, the developed electrode shows excellent sensitivity (0.76 nA mM^{-1}), low limit of detection (0.2 nM based on 3σ) and wide linear range (50–1000 nM). The obtained results are in great competition with the reported literature, thus suggesting the reliability of our designed electrode (Table S5†). The high sensing efficacy of the developed electrode could be attributed to:

(i) Existence of a greater fraction of catalytic active sites because of the generation of enhanced graphitic C and the number of surface defects as evidenced by Raman results (Fig. S4A†). These defects offer fast and smooth transportation of ions at the electrode–electrolyte interface.[21]

(ii) Strong binding interaction (H-bonding) between the PDA/IL redox mediator and NC@Au-NPs offers fast and smooth pathways for fast transportation of ions.

(iii) Synergetic effect of highly electroactive NC@Au-NPs with a highly conductive PDA/IL redox mediator, which acts as
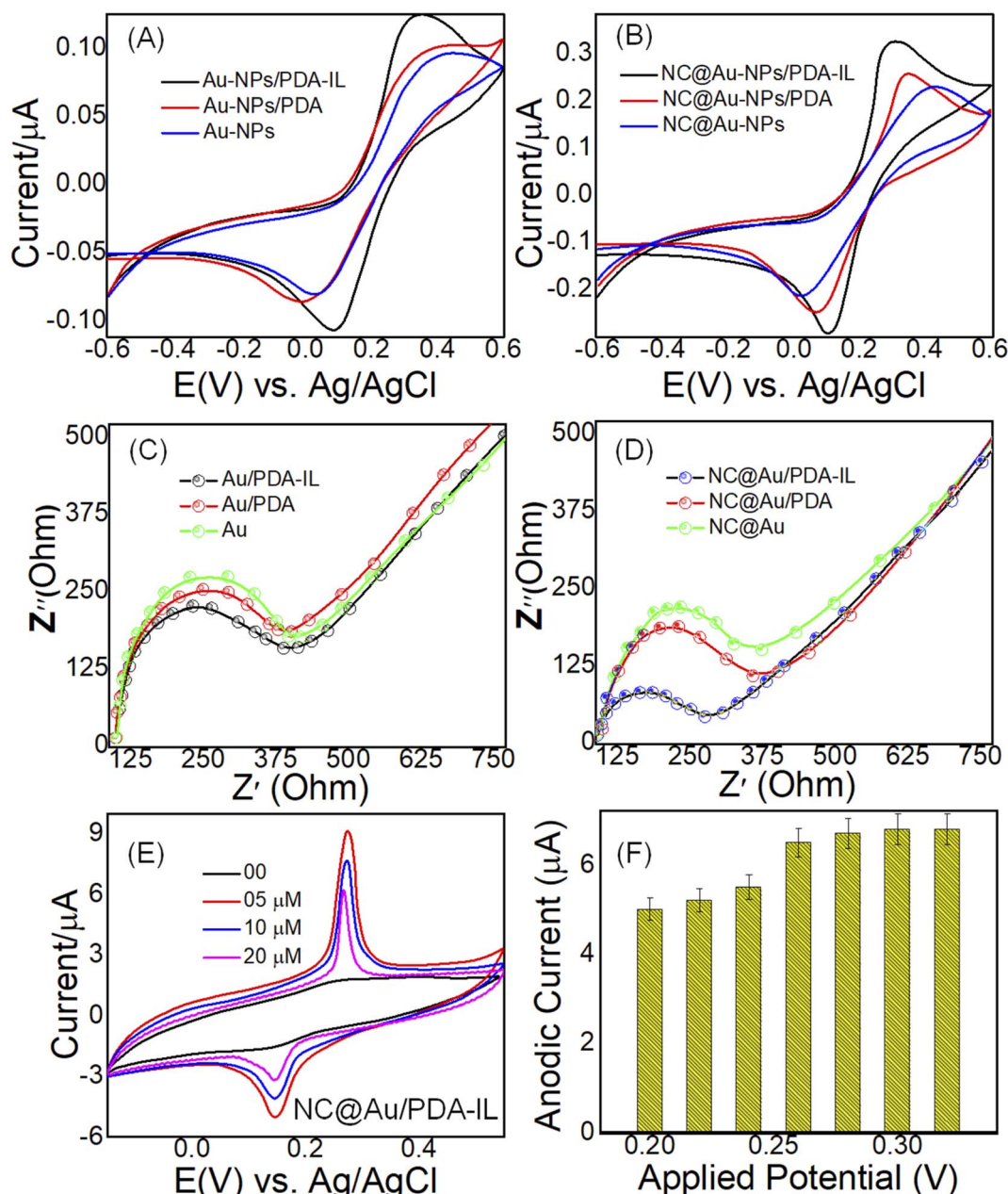

Fig. 3 CV-based electrochemical behavior of (A) Au-NPs, Au-NPs/PDA, and Au-NPs/PDA–IL, and (B) NC@Au-NPs, NC@Au-NPs/PDA, and NC@Au-NPs/PDA–IL electrodes at a scan rate of 100 mV s^{-1} towards 2 mM of [Fe$_6$]$^{3-/4-}$ (ref. 31). Nyquist plots of (C) Au-NPs, Au-NPs/PDA, and Au-NPs/PDA–IL, and (D) NC@Au-NPs, NC@Au-NPs/PDA, and NC@Au-NPs/PDA–IL electrodes using the [Fe$_6$]$^{3-/4-}$ (ref. 31) as redox probe. (E) CV of NC@Au-NPs/PDA–IL based electrode towards increasing doses of DA in 0.1 M PBS (pH: 7). (F) Optimization of the applied potential at the NC@Au-NPs/PDA/IL electrode towards DA monitoring.
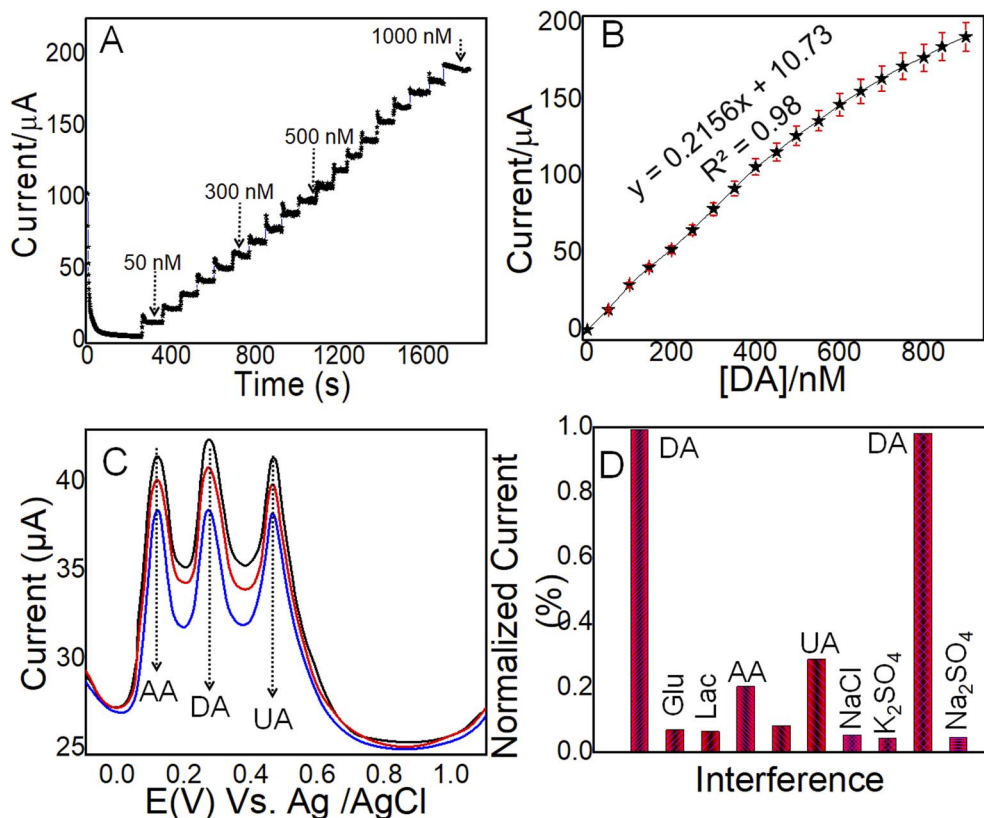
Fig. 4 (A) Amperometric current response of the Au-NPs/PDA–IL electrode at the increasing concentration (50–1000 nM) of DA in PBS (pH 7.0) at 0.26 V at a constant stirring speed of 300 rpm, and its linear calibration graph (B) derived from amperometric results (A). (C) DPV-based selective efficacy of the Au-NPs/PDA–IL electrode at increasing concentrations of DA (10, 20 and 30 μM) along with interferents such as AA and UA (20, 40 and 60 μM), respectively. (D) Normalized selective electrochemical current response of the Au-NPs/PDA–IL electrode derived from amperometric measurements towards DA even in the presence of organic (DA, AA, UA, and Lac) and inorganic (KCl, NaCl, Na₂SO₄, and K₂SO₄) interferents.

a booster to provide high π-electron density because of the availability of aromatic rings and carboxyl functional groups.[34]

The real-time determination of the DA sensor is mainly dependent on the selective efficacy of the designed electrode. Thus, differential pulse voltammetry (DPV) and amperometry were applied to monitor the selective efficacy of the designed NC@Au-NPs/PDA/IL electrode. Fig. 4C shows the DPV current response of the NC@Au-NPs/PDA/IL electrode towards increasing doses of DA (10, 20, and 30 μM) along with increasing concentrations (20, 40, and 60 μM) of highly interfering agents including UA and AA. It is evident from the results that the DPV peak current of all three analytes increased with the increase in concentration at their respective oxidation peak potential values with a prominent peak potential value. These results indicate reliable selective efficacy of the developed electrode.

However, the evaluation of selective efficacy in the presence of various organic and inorganic species is also important in developing a sensor to be applicable for real-time monitoring. Thus, we performed amperometric measurements at a constant potential (0.26 V) to record the selective efficacy of the designed NC@Au-NPs/PDA/IL electrode towards DA and co-existing electroactive species such as inorganic (KCl, NaCl, Na₂SO₄,

and K₂SO₄) and organic (DA, AA, UA, Glu and Lac) in 0.1 M PBS (pH: 7) electrolyte (Fig. S9†). Moreover, Fig. 4D shows the normalized current response derived from Fig. S9,† clearly indicating the excellent selective efficacy of the designed electrode. The excellent selectivity of the developed electrode could be attributed to:

(i) The existence of exposition of more fractions of catalytic active sites and surface defects along with short diffusion pathways allows the fast transportation of ions at the NC@Au-NPs/PDA/IL electrode surface and to oxidize the analyte at its specific oxidation potential as evidenced by Fig. 4C.

(ii) It has been reported that neurotransmitters generally exist in cationic form with a positive charge at physiological pH.[35] Thus, the strongly interacted redox mediator at the surface of NC@Au-NPs offers suitable accommodation and binding spaces to the positively charged[36] DA at its specific oxidation potential as evident from Fig. S5.†

3.6 Reproducibility and reusability of NC@Au-NPs/PDA/IL-based electrodes

Reproducibility and reusability of any sensor are of great importance to meet future demands. Thus, herein, amperometric analysis was performed to assess the reproducibility of
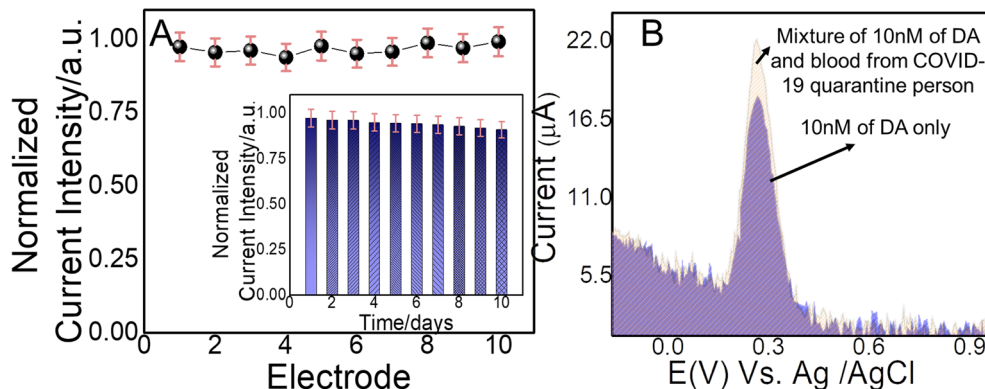
Fig. 5 (A) Reproducible amperometric current response of 10 different Au-NPs/PDA–IL-based electrodes towards 50 nM of DA (*vs.* Ag/AgCl). The inset shows the long-term stability of the Au-NPs/PDA–IL electrode-based electrode for continuous 10 days towards electrochemical oxidation of fixed concentration (50 nM) of DA by amperometry. (B) DPV current response of Au-NPs/PDA–IL-based electrodes to additions of 10 nM of DA and mixture of 10 nM of DA along with 20 μL of blood.

the established NC@Au-NPs/PDA/IL electrode towards DA in terms of electrode-to-electrode reproducible efficacy and reusability. In such kind of experimental analysis, amperometric current responses have been studied for multiple (≥10) developed electrodes towards constant concentration of DA (50 nM) under optimum sensing conditions in 0.1 M PBS (pH: 7) at an applied potential of 0.26 V (*vs.* Ag/AgCl) and room temperature. The findings revealed that the reproducibility of 10 electrodes demonstrates RSD between 2.67 and 4.55%, as testified by the plotting response current graphs (Fig. 5A). Similarly, the inset in Fig. 5A shows the reusability of designed electrodes over 10 days against constant doses of DA (50 nM). The findings show that even after 10 days, the designed electrode has retained more than 93% of sensing efficacy, thus suggesting the reliable, reproducible, and reusable efficacy of the designed electrode.

3.7 Applicability of the NC@Au-NPs/PDA/IL-based electrode towards DA screening in the blood of a COVID-19 quarantined volunteer

The rate of increase of neurological disorders such as depression, anxiety, delirium, and agitation has become double or even more after the COVID-19 outbreak. Alarmingly, the neurological disorders become more vulnerable in peoples having already some neurological disorders after COVID-19 quarantine. Therefore, highly sensitive and selective monitoring of DA in the blood of COVID-19 quarantined patients has gained considerable interest. Thus, here, we measured the DA level in the blood of a 30 year-old COVID-19 quarantined volunteer.

To evaluate the real-time physical applicability, the designed (NC@Au-NPs/PDA/IL) electrode was applied against the human blood sample of COVID-19 quarantined patients with unknown DA concentration and spiked it a known concentration of DA. A highly sensitive and selective DPV technique was applied to monitor the current response of NC@Au-NPs/PDA/IL towards the spiked blood sample of COVID-19 quarantined patients and compared it with the results of standard sample of DA. Fig. 5B clearly depicts the DPV response of the developed electrode

towards 10 nM of DA standard solution with a current magnitude of ~18.17 μA, whereas the DPV current response raised to ~21.07 μA towards the mixture (10 nM of DA and 20 μL of blood). Thus, an increase in current in case of DA-mixed COVID-19 quarantined patient blood sample indicates the reliable sensing efficacy of our designed sensor for real biological samples and demonstrates the developed system's durability for future prospective.

To validate the capability of the designed sensor, the developed sensor was further applied to monitor the DA from pharmaceutical products such as dopamine hydrochloride injection. We applied the standard addition method for the real-time monitoring of DA. Briefly, the dopamine hydrochloride injection was first diluted in 0.1 M PBS (pH: 7). Next, we measure the DPV response of the designed NC@Au-NPs/PDA/IL electrode towards three different amounts of the diluted dopamine hydrochloride samples. The results (Table S6†) obtained from the recovery tests indicate the reliability and accuracy of the developed electrode.

4. Conclusion

In summary, we reported the fabrication of a novel electrochemical sensor for DA monitoring in COVID-19 quarantined patient and pharmaceutical samples by using a NC@Au/PDA–IL/GPE hybrid electrode. The designed sensor shows an excellent limit of detection of 0.002 μM and reliable shelf life towards DA, thus making it suitable to monitor and understand DA-based health issues. It is proposed that the strong electrostatic interaction between DA and the electrode surface leads to fast electron transfer at the interface, which is further boosted *via* strongly interacted π-electron-rich highly conductive PDA/IL redox mediator. To the best of our knowledge, this is the first report to use a NC@Au/PDA–IL hybrid electrode for the sensitive and selective monitoring of DA in COVID-19 quarantined patients. The designed NC@Au/PDA–IL/GPE hybrid electrode shows great potential in developing diagnostic devices for future advancements.

Ethical statement

All experiments were performed in compliance with the relevant laws and institutional guidelines and have been approved by IRB/IEC (Institutional review Board/Independent Ethical Committee) Ibn e Siena Research Institute, Multan Medical & Dental College, Multan Pakistan (Ref. Publi/01/22). All donors had given their informed consent according to the guidelines of the ethical committee specified above.

Conflicts of interest

There are no conflicts to declare.

Acknowledgements

References

1 A. Vittori, J. Lerman, M. Cascella, A. D. Gomez-Morad, G. Marchetti, F. Marinangeli and S. G. Picardo, *Anesth. Analg.*, 2020, **131**, 117–119.

2 A. Sharma, S. Tiwari, M. K. Deb and J. L. Marty, *Int. J. Antimicrob. Agents*, 2020, **56**, 106054.

3 I. Chakraborty and P. Maity, *Sci. Total Environ.*, 2020, **728**, 138882.

4 T. Masood, M. Asad, S. Riaz, N. Akhtar, A. Hayat, M. A. Shenashen and M. M. Rahman, *Mater. Chem. Phys.*, 2022, **289**, 126451.

5 A. Fiorillo and P. Gorwood, *Eur. Psychiatry*, 2020, **63**, e32.

6 A. Munawar, F. Zafar, S. Majeed, M. Irfan, H. U. Khan, G. Yasmin and N. Akhtar, *J. Electroanal. Chem.*, 2021, **895**, 115469.

7 M. Asad, A. Zulfiqar, R. Raza, M. Yang, A. Hayat and N. Akhtar, *Electroanalysis*, 2020, **32**, 11–18.

8 M. Y. Emran, M. A. Shenashen, M. Mekawy, A. M. Azzam, N. Akhtar, H. Gomaa, M. M. Selim, A. Faheem and S. A. El-Safty, *Sens. Actuators, B*, 2018, **259**, 114–124.

9 M. Y. Emran, M. Mekawy, N. Akhtar, M. A. Shenashen, I. M. El-Sewify, A. Faheem and S. A. El-Safty, *Biosens. Bioelectron.*, 2018, **100**, 122–131.

10 M. Y. Emran, H. Khalifa, H. Gomaa, M. A. Shenashen, N. Akhtar, M. Mekawy, A. Faheem and S. A. El-Safty, *Microchim. Acta*, 2017, **184**, 4553–4562.

11 N. Akhtar, M. Y. Emran, M. A. Shenashen, H. Khalifa, T. Osaka, A. Faheem, T. Homma, H. Kawarada and S. A. El-Safty, *J. Mater. Chem. B*, 2017, **5**, 7985–7996.

12 M. Pierce, H. Hope, T. Ford, S. Hatch, M. Hotopf, A. John, E. Kontopantelis, R. Webb, S. Wessely, S. McManus and K. M. Abel, *Lancet Psychiatry*, 2020, **7**, 883–892.

13 M. Y. Emran, M. A. Shenashen, A. A. Abdelwahab, H. Khalifa, M. Mekawy, N. Akhtar, M. Abdelmottaleb and S. A. El-Safty, *J. Appl. Electrochem.*, 2018, **48**, 529–542.

14 R. Franco, I. Reyes-Resina and G. Navarro, *Biomedicines*, 2021, **9**(2), 109.

15 K. Hayat, A. Munawar, A. Zulfiqar, M. H. Akhtar, H. B. Ahmad, Z. Shafiq, M. Akram, A. S. Saleemi and N. Akhtar, *ACS Appl. Mater. Interfaces*, 2020, **12**, 47320–47329.

16 K. Hayat, M. Hassan Akhtar, A. Siddique Saleemi, H. Badaruddin Ahmad and N. Akhtar, *Electroanalysis*, 2020, **32**, 1664–1670.

17 D.-J. Park, J.-H. Choi, W.-J. Lee, S. H. Um and B.-K. Oh, *J. Nanosci. Nanotechnol.*, 2017, **17**, 8012–8018.

18 T. D. Thanh, J. Balamurugan, S. H. Lee, N. H. Kim and J. H. Lee, *Biosens. Bioelectron.*, 2016, **81**, 259–267.

19 S. Mahalakshmi and V. Sridevi, *Electrocatalysis*, 2021, **12**, 415–435.

20 L. Yang, T. Wang, C. Bao, M. Shi, X. Huang and H. Cheng, *J. Electroanal. Chem.*, 2021, 115512.

21 A. S. Saleemi, M. Hafeez, A. Munawar, N. Akhtar, W. Abbas, M. E. Mazhar, Z. Shafiq, A. P. Davis and S.-L. Lee, *J. Mater. Chem. C*, 2020, **8**, 12984–12992.

22 K. Vuorensola, H. Sirén and U. Karjalainen, *J. Chromatogr. B: Anal. Technol. Biomed. Life Sci.*, 2003, **788**(2), 277–289.

23 W. Abbas, N. Akhtar, Q. Liu, T. Li, I. Zada, L. Yao, R. Naz, W. Zhang, M. E. Mazhar and D. Zhang, *Sens. Actuators, B*, 2019, **282**, 617–625.

24 A. K. Sahu and S. Raj, 2020.

25 A. S. Saleemi, M. Hafeez, A. Munawar, N. Akhtar, W. Abbas, M. E. Mazhar, Z. Shafiq, A. P. Davis and S.-L. Lee, *J. Mater. Chem. C*, 2020, **8**, 12984–12992.

26 A. Noruozi and A. Nezamzadeh-Ejhieh, *Chem. Phys. Lett.*, 2020, **752**, 137587.

27 S. Govindaraju, M. Ramasamy, R. Baskaran, S. J. Ahn and K. Yun, *Int. J. Nanomed.*, 2015, **10**(Spec Iss), 67–78.

28 J. B. Lambert, H. F. Shurvell, D. A. Lightner and R. G. Cooks, *Introduction to organic spectroscopy*, Macmillan Publishing Company, 1987.

29 C. G. Núñez, J. Pau, M. Hernández, M. Cervera and J. Piqueras, 2011.

30 S. Kumar, A. Sindhu and P. Venkatesu, *ACS Appl. Nano Mater.*, 2021, **4**, 3185–3196.

31 B. Gavin, J. Lyne and F. McNicholas, *Ir. J. Psychol. Med.*, 2020, **37**, 156–158.

32 T. A. Silva, H. Zanin, E. Saito, R. A. Medeiros, F. C. Vicentini, E. J. Corat and O. Fatibello-Filho, *Electrochim. Acta*, 2014, **119**, 114–119.

33 J. F. Gomes, L. H. S. Gasparotto and G. Tremiliosi-Filho, *Phys. Chem. Chem. Phys.*, 2013, **15**, 10339–10349.

34 Y. Abbas, S. Ali, M. Basharat, W. Zou, F. Yang, W. Liu, S. Zhang, Z. Wu, N. Akhtar and D. Wu, *ACS Appl. Nano Mater.*, 2020, **3**, 11383–11390.

35 C. Gong, W. Wang, K. Bowen and X. Zhang, *J. Phys. Chem. B*, 2019, **123**, 7695–7699.

36 S. Thirumalairajan, K. Girija, V. Ganesh, D. Mangalaraj, C. Viswanathan and N. Ponpandian, *Cryst. Growth Des.*, 2013, **13**, 291–302.